Author Manuscript

Author Manuscript

Author Manuscript

Author Manuscript

HHS Public Access

Author manuscript

Cell Rep. Author manuscript; available in PMC 2022 September 20.

Published in final edited form as:

Cell Rep. 2021 November 02; 37(5): 109925. doi:10.1016/j.celrep.2021.109925.

Inverse neurovascular coupling contributes to positive feedback excitation of vasopressin neurons during a systemic homeostatic challenge

Ranjan K. Roy[1], **Ferdinand Althammer**[1], **Alexander J. Seymour**[2], **Wenting Du**[3], **Vinicia C. Biancardi**[4], **Jordan P. Hamm**[1], **Jessica A. Filosa**[3], **Colin H. Brown**[2], **Javier E. Stern**[1,5,*]

[1]Neuroscience Institute, Georgia State University, Atlanta, GA, USA

[2]Department of Physiology, University of Otago, Dunedin, New Zealand

[3]Department of Physiology, Augusta University, Augusta, GA, USA

[4]Department of Anatomy, Physiology and Pharmacology, Auburn University, Auburn, AL, USA

[5]Lead contact

SUMMARY

Neurovascular coupling (NVC), the process that links neuronal activity to cerebral blood flow changes, has been mainly studied in superficial brain areas, namely the neocortex. Whether the conventional, rapid, and spatially restricted NVC response can be generalized to deeper and functionally diverse brain regions remains unknown. Implementing an approach for *in vivo* two-photon imaging from the ventral surface of the brain, we show that a systemic homeostatic challenge, acute salt loading, progressively increases hypothalamic vasopressin (VP) neuronal firing and evokes a vasoconstriction that reduces local blood flow. Vasoconstrictions are blocked by topical application of a VP receptor antagonist or tetrodotoxin, supporting mediation by activity-dependent, dendritically released VP. Salt-induced inverse NVC results in a local hypoxic microenvironment, which evokes positive feedback excitation of VP neurons. Our results reveal a physiological mechanism by which inverse NVC responses regulate systemic homeostasis, further supporting the notion of brain heterogeneity in NVC responses.

In brief

This is an open access article under the CC BY-NC-ND license (http://creativecommons.org/licenses/by-nc-nd/4.0/).

*Correspondence: jstern@gsu.edu.

AUTHOR CONTRIBUTIONS

J.E.S., J.A.F., and C.H.B. conceived and planned the experiments. R.K.R., J.E.S., and C.H.B. performed *in vivo* imaging experiments and p02 measurements. J.P.H. assisted with the planning and execution of *in vivo* imaging experiments. J.A.F. and W.D. performed *ex vivo* electrophysiological recordings. C.H.B. and A.J.S. performed *in vivo* electrophysiological recordings. V.C.B. performed cardiovascular monitoring and blood gas sample collection and analysis. F.A. and R.K.R. performed qPCR studies. J.E.S., C.H.B., J.A.F., and R.K.R. wrote the paper with input from all authors.

DECLARATION OF INTERESTS

The authors declare no competing interests.

SUPPLEMENTAL INFORMATION

Supplemental information can be found online at https://doi.org/10.1016/j.celrep.2021.109925.

Author Manuscript Author Manuscript Author Manuscript Author Manuscript

Using *in vivo* two-photon imaging from the ventral surface of the brain, Roy et al. show that the systemic homeostatic challenge of acute salt loading evokes activity-dependent vasoconstrictions in the SON. This causes a hypoxic, pro-excitatory milieu, which induces positive feedback excitation of VP neuronal activity during the homeostatic challenge.

Graphical Abstract

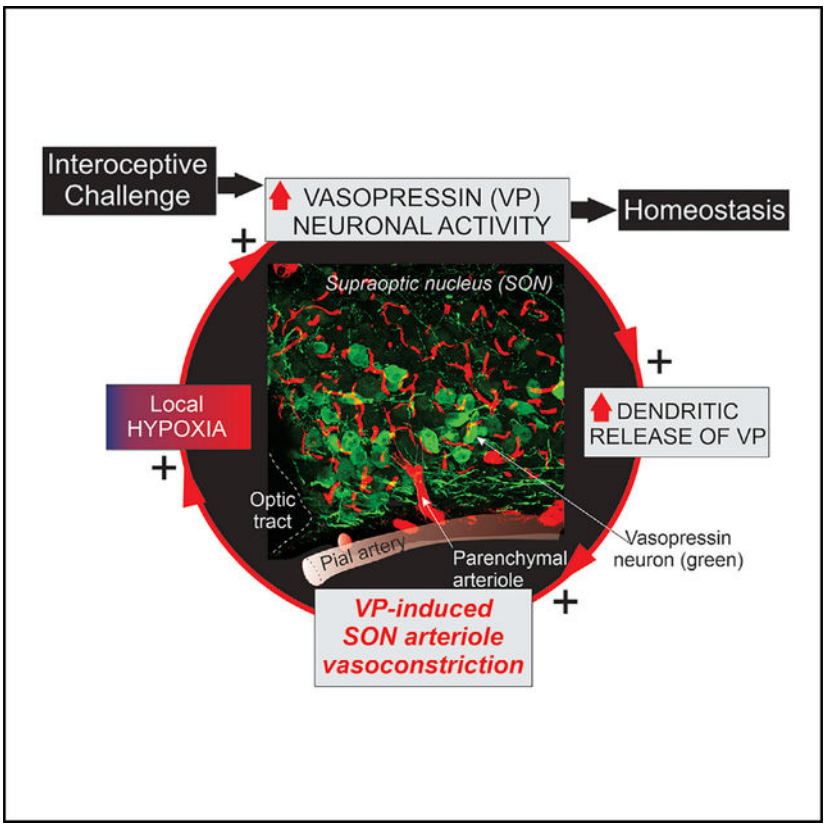

INTRODUCTION

Tight coupling between neuronal activity and cerebral blood flow (CBF) ensures optimal delivery of glucose and oxygen to brain areas with increased metabolic demand, a process termed neurovascular coupling (NVC) (Iadecola, 2017). The use of high-resolution *in vivo* imaging approaches, coupled with genetically encoded indicators, has enabled remarkable advances in understanding the intercellular mechanisms mediating NVC responses (Iadecola, 2017; Urban et al., 2017). However, such studies have been mainly limited to superficial dorsal brain areas, particularly the cortex and in response to specific sensory events, where neuronal-activity-evoked CBF changes occur rapidly (<2 s) and in a spatially restricted manner (Li et al., 2009; Silva et al., 2000). This has led to the prevailing view that NVC is a uniform process across brain regions. However, *in vivo* evidence supporting this is lacking. Importantly, factors that modulate the NVC response, such as the structural-functional organization of the neurovascular unit, inputs from subcortical areas, vascular density, and metabolic demands, vary considerably across brain regions (Acer

Author Manuscript Author Manuscript Author Manuscript Author Manuscript

et al., 2008; Cauli and Hamel, 2010; Devonshire et al., 2012; Vázquez-Rodríguez et al., 2019), suggesting that NVC could be region specific. To address this question, we used the hypothalamic supraoptic nucleus (SON) as a model to measure *in vivo* NVC in a brain region that is anatomically and functionally distinct from the cortex.

The SON houses a population of neuropeptidergic neurons that express vasopressin (VP). In response to changes in fluid and electrolyte levels, such as salt loading, an approach that emulates the physiological consequences of a high-salt meal, VP neurons fire action potentials. Consequently, VP is released from the posterior pituitary gland into the circulation, resulting in a progressive and sustained increase of plasma VP, needed to restore and maintain body fluid homeostasis (Bourque et al., 2007; Verbalis, 2003). Notably, VP neuron activation and the increased metabolic demands of the SON in response to this interoceptive systemic challenge are slow, long lasting, and encompass the entire population of VPergic neurons (Leng et al., 2008), displaying thus an overall distinct spatiotemporal dynamic compared to the characteristic rapid sensory-evoked response reported in cortical brain regions.

VP is also locally released from the dendrites of SON neurons in an activity-dependent manner (Brown et al., 2020; Ludwig and Leng, 2006). Dendritically released VP has autocrine, paracrine, and hormone-like actions that affect not only the firing activity of VP neurons (Gouzènes et al., 1998) but also the activity of relatively distant neuronal (Son et al., 2013), astrocytic (Haam et al., 2014), and vascular (Du et al., 2015) targets.

The SON is a deep brain region with unique cytoarchitectural properties (Hatton, 1997), including a high vascularization (Ambach and Palkovits, 1974; Badaut et al., 2000). Paradoxically, the dense vascular network is not required to maintain its metabolic demands (Badaut et al., 2000; Weber et al., 2008). This mismatch in metabolic supply and demand suggests that the SON vasculature may serve additional functions beyond the delivery of energy substrates.

Based on all of the above, we tested the hypothesis that, in the SON, the NVC response serves to amplify neuronal responses needed to maintain body fluid homeostasis. Using *in vivo* electrophysiology along with a newly developed *in vivo* two-photon imaging approach that enables optical access to the ventral hypothalamus, we show that activity-dependent dendritic VP release in response to a systemic homeostatic challenge, an acute salt load, evokes a distinct physiological form of NVC in the SON. The latter was characterized by a slow and sustained vasoconstriction that decreased blood flow (called here inverse NVC). We provide evidence that this unique NVC modality results in a local hypoxic microenvironment, which sustains the elevated VP neuronal activity needed to restore body fluid homeostasis in response to the systemic challenge.

Author Manuscript Author Manuscript Author Manuscript Author Manuscript

RESULTS

Neuronal and vascular cytoarchitecture of the SON revealed by *in vivo* two-photon imaging

A schematic of the hypothalamic preparation is shown in Figures 1A and 1C. The SON was readily identified by the presence of EGFP-VP-expressing neurons that had elongated somata and highly varicose dendritic and axonal processes (Figures 1J–1S).

To differentiate SON arterioles from venules, rats were given an intravenous (i.v.) injection of the artery-specific dye Alexa Fluor 633 (Shen et al., 2012) to pre-label pial and parenchymal arterioles (Figures 1D–1F) before vascular filling after i.v. administration of rhodamine or fluorescein 70 kDa dextran. There was a clear delay between the filling of Alexa Fluor 633 pre-labeled arterioles and non-labeled veins (Figures 1G–1I; Video S1).

Vascular filling revealed a distinct angioarchitecture (Figures 1B and S1A–S1D) with the visually accessible area of the SON located medially to the bifurcation of the internal carotid artery (ICA), one of the main pial vessels supplying the SON (Ambach and Palkovits, 1979) and the middle cerebral artery (MCA). ICA-branching arterioles (perforating arterioles) emerged near the most caudal aspect of the SON (~100 μm deep from the brain surface), where they branched into smaller arterioles, contributing to a dense capillary network (~5.55 μm diameter; ~160 μm deep). A large venule (~60 μm diameter; ~170 μm deep) and several smaller venules were also observed within the SON. Finally, a set of smaller (~18.5 μm) and deeper arterioles (~220 μm deep), possibly originating from the ICA, were observed medial to the SON.

Salt loading evokes a sustained increase in vasopressin neuronal activity along with vasoconstriction of pial and SON parenchymal arterioles

To determine whether SON VP neuronal activation in response to an acute salt load evokes NVC, rats were subjected to a slow i.v. infusion of hypertonic saline (HTS) (2 M NaCl, 33 μL/min, 30 min). Plasma osmolarity was higher in HTS-infused versus isotonic-saline-infused animals (isotonic: 304.5 ± 1.2 mOsm/L; HTS: 345.8 ± 3.2 mOsm/L; $n = 5$ rats; $p < 0.001$; unpaired t test). Cerebrospinal fluid (CSF) osmolarity was also higher in HTS-infused than in isotonic-saline-infused animals (isotonic: 297.4 ± 2.8 mOsm/L; HTS: 343.2 ± 1.24 mOsm/L; $n = 5$ rats each; $p < 0.0001$; unpaired t test).

Similar to previously published data (Leng et al., 2001), we found that HTS evoked a gradual and linear increase in the firing rate of VP neurons ($p < 0.0001$; one-way repeated-measures [RM] ANOVA; $n = 4$ cells from 4 rats; Figure 2A), displaying a relatively rapid onset and peaking ~30 min from stimulus onset.

In vivo time series two-photon imaging of the SON vasculature during the same HTS infusion revealed significant arteriole vasoconstrictions (Figures 2B–2I) without evoking changes in systemic physiological parameters, including mean arterial pressure, heart rate, and blood gases when compared to isotonic saline infusion (Figure S2; $n = 4$ rats in each group). Comparable peak constrictions were observed both in ICAs (one-way RM ANOVA; $p < 0.05$; $n = 5$ vessels from 5 rats) and perforating arterioles (RM one-way ANOVA; $p < 0.0001$; $n = 13$ vessels from 5 rats; Figure 2I). In contrast, no changes in venule diameter

Author Manuscript Author Manuscript Author Manuscript Author Manuscript

were observed (one-way RM ANOVA; $p = 0.75$; $n = 9$ vessels from 5 rats). The onset of the vasoconstriction occurred at 4.0 ± 1.0 min and 3.7 ± 0.6 min for ICAs and perforating arterioles, respectively ($p = 0.50$; paired t test), and progressively developed, reaching a plateau ~12–16 min from the HTS onset. Although a slow recovery was observed thereafter, vasoconstriction persisted throughout the HTS infusion and was observed in all arterioles, independent of their initial diameters ($r^2 = 0.17$; $p = 0.20$).

Infusion of isotonic saline did not evoke vascular responses in ICAs (RM one-way ANOVA; $p = 0.97$; $n = 3$ vessels from 3 rats), perforating arterioles (one-way RM ANOVA; $p = 0.37$; $n = 8$ vessels from 3 rats), or venules (one-way RM ANOVA; $p = 0.42$; $n = 8$ vessels from 3 rats; Figures S3A and S3B).

To determine whether HTS-induced vascular responses were activity dependent, experiments were repeated following the topical application of the Na^+ channel blocker, tetrodotoxin (TTX) (1 μM). We found that HTS infusion failed to evoke a vascular response in perforating arterioles (one-way RM ANOVA; $p = 0.21$; $n = 5$ vessels from 3 rats) or venules (one-way RM ANOVA; $p = 0.16$; $n = 7$ vessels from 3 rats) in the presence of TTX (Figures S3C–S3F).

Local dendritic release of VP mediates hypertonic-saline-induced vasoconstriction in the SON

High-resolution, two-photon imaging revealed an intimate physical association between EGFP-VP neurons and the labeled microvasculature (Figures 3A–3H). Capillaries enwrapped individual EGFP-VP neurons, which in many instances were found in close apposition to parenchymal arterioles. Moreover, varicose processes containing highly stained EGFP-VP were seen to run along and in close apposition to these vessels. Based on these anatomical observations and the established knowledge of activity-dependent dendritic VP release and that VP is a potent vasoconstrictor (Yosten and Samson, 2012), we then examined whether HTS-evoked vasoconstrictions were mediated by dendritically released VP.

HTS-induced vascular responses were measured in the presence of the V1a receptor antagonist (β-mercapto-β,β-cyclopentamethylenepropionyl^1, [O-me-Tyr^2, Arg^8]-VP, 1 μM) topically applied to the SON. The V1aR antagonist abolished HTS-induced vasoconstrictions in ICAs and SON-perforating arterioles and unmasked vasodilations in ICAs (one-way RM ANOVA; $p < 0.0001$; $n = 4$ vessels from 4 rats; Figures 3J–3O), with a mean onset at 7.5 ± 2.9 min. A trend toward vasodilation was evident in perforating arterioles but did not reach statistical significance (one-way RM ANOVA; $p = 0.10$; $n = 5$ vessels from 4 rats). No responses to HTS were observed in venules (one-way RM ANOVA; $p = 0.99$; $n = 7$ vessels from 4 rats; Figure 3P).

Taken together, these results suggest that activity-dependent dendritic VP release evokes pronounced arteriole vasoconstrictions in response to an acute salt load. Moreover, blockade of VP-mediated vasoconstriction unveiled an underlying activity-dependent vasodilation.

Author Manuscript Author Manuscript Author Manuscript Author Manuscript

Salt load decreases in blood flow are associated with tissue hypoxia and increased firing activity of vasopressin neurons

To determine whether the HTS-induced vasoconstriction decreased blood flow within the SON microcirculation, we measured red blood cell (RBC) velocities during HTS infusion. As shown in Figures 4A and 4B, a progressive decrease in RBC velocity was observed in contiguous SON-perforating arterioles (−41.5% ± 2.2%; one-way RM ANOVA; $p < 0.0001$; n = 4 vessels from 4 rats) and venules (−32.6% ± 4.1%; one-way RM ANOVA; $p < 0.001$; n = 4 vessels from 4 rats). RBC velocity also decreased significantly in SON capillaries (one-way RM ANOVA; $p < 0.0001$; n = 17 vessels from 6 rats; Figure S4).

To assess whether HTS-induced decreases in blood flow resulted in local tissue hypoxia, we directly monitored SON tissue partial pressure of oxygen (pO_2) before and during an isotonic or HTS infusion. Baseline pO_2 in the SON was 35.8 ± 3.7 mmHg (n = 12). HTS resulted in a rapid and progressive decrease in SON pO_2 (one-way RM ANOVA; $p < 0.002$; n = 6 rats; Figures 4C and 4D). Conversely, infusion of isotonic saline failed to change SON pO_2 (one-way RM ANOVA; $p = 0.6$; n = 4 rats; Figure 4D). Importantly, when experiments were repeated in the presence of the V1a receptor antagonist, a progressive increase in SON pO_2 was observed (one-way RM ANOVA; $p < 0.002$; n = 4 rats; Figure 4D). Recovery in the pO_2 response was observed when a shorter (6 min; n = 4 rats) HTS infusion period was tested (Figure S5). These data further support the induction of a VP-mediated hypoxic milieu following hypertonic stimulation in the SON.

In addition, we performed qPCR for the hypoxia inducible factor (HIF)-1α mRNA, an established marker of tissue hypoxia (Choudhry and Harris, 2018). Unilateral ligation of the ICA increased HIF-1α mRNA levels by ~7-fold in the ipsilateral SON when normalized to the contralateral control side ($p < 0.01$; one-sample t test against the hypothetical mean ± 1; n = 6 rats; Figure 4E), corroborating that the ICA region imaged in our functional studies supplies the SON. In response to hypertonic saline infusion, SON HIF-1α mRNA increased by ~2.5-fold compared to an isotonic saline infusion ($p < 0.001$; one-sample t test against the hypothetical mean ± 1; n = 6 rats; Figure 4E).

To determine the functional consequences of the tissue hypoxia on VP neuron activity, we obtained patch-clamp recordings from EGFP-VP neurons in slices. We found that transient hypoxia (from 95% O_2 to 20% O_2 aCSF for 8 min) increased VP neuron firing rate (~85% increase; $p < 0.02$; paired t test; n = 14 cells from 10 rats; Figures 4F and 4G).

Taken together, these data suggest that vasoconstriction induced in response to an acute salt load decreases blood flow and induces local hypoxia within the SON, which amplifies the increase in VP neuron activity triggered by the systemic challenge.

DISCUSSION

Using an innovative surgical approach in conjunction with *in vivo* two-photon imaging of the ventral surface of the brain, we show that an acute systemic salt load induced vasoconstriction of parenchymal and pial arterioles perfusing the SON. The salt-induced vasoconstriction was activity dependent and mediated by endogenous, dendritic release

Author Manuscript Author Manuscript Author Manuscript Author Manuscript

VP acting on V1a receptors. Blockade of V1a receptors unmasked an underlying activity-dependent vasodilation. The salt-induced vasoconstriction decreased blood flow in the SON sufficiently to decrease oxygen supply and generate local hypoxia, which, *ex vivo*, increased the activity of VP neurons. Collectively, these results indicate that an acute salt challenge increases dendritic VP release within the SON to evoke an atypical, yet functionally relevant, inverse NVC response. We propose this unique NVC response contributes to a local positive-feedback signaling mechanism that underpins sustained increases in the activity of the VP neuronal population, a critical step in the homeostatic response to the salt-induced systemic challenge.

Inverse neurovascular coupling contributes to an integrative physiological homeostatic response

Vasoconstrictions have been previously reported as part of complex NVC responses to sensory-evoked stimuli (e.g., vasodilations followed by vasoconstrictions; Cai et al., 2018; Devor et al., 2007, 2008; Tian et al., 2010), in response to the stimulation of specific brain regions (e.g., locus coeruleus; de la Torre, 1976), signaling pathways (e.g., purinergic signaling; Cai et al., 2018), or selective neuronal populations (Cauli et al., 2004; Perrenoud et al., 2012; Uhlirova et al., 2016). In addition, robust activity-dependent decreases in CBF, sometimes referred to as inverse NVC, are deemed part of a pathological response seen under conditions of metabolic-supply mismatch, such as cortical spreading depression, ischemia, and subarachnoid hemorrhage (Balbi et al., 2017; Bere et al., 2014; Hinzman et al., 2014). Here, we report a physiological form of inverse NVC evoked by an interoceptive physiological process involving a brain region crucial for maintenance of whole-body homeostasis. Specifically, we show that an acute systemic salt load, a challenge that activates SON VP neurons and results in both the systemic and intranuclear release of VP (Ludwig et al., 1994), evoked vasoconstriction of a broad range of vessels perfusing the SON. These included a main pial artery, the ICA, and corresponding branches (perforating arterioles), which penetrate the brain parenchyma of this region. Consequently, blood flow in downstream capillaries and venules was reduced.

Contrary to the conventional NVC response, the inverse NVC observed in the SON was slow, sustained, and widespread, as it affected vessels distant from the site of VP-expressing neurons. Importantly, SON vascular responses to the acute salt load displayed similar temporal kinetics to that of the firing activity of the VP neuronal population when subjected to the same stimulus.

Hypothalamic homeostatic responses, such as those mediated by the VPergic system in response to a salt challenge, require the activation of the entire neuronal population and must be sustained throughout the perturbation (Leng et al., 2008). Moreover, ion and fluid homeostatic challenges evoke complex multi-modal responses (Bourque, 2008), involving interpopulation crosstalk between VP neurons and presympathetic neurons, mediated by dendritic release of VP and slow diffusion in the extracellular space (Son et al., 2013). Thus, the slow and widespread nature of the inverse NVC response evoked by a systemic salt load is aligned with the dynamics of this neuronal network.

Author Manuscript Author Manuscript Author Manuscript Author Manuscript

However, the inverse polarity of the salt-induced vascular response unveiled in this study was unexpected, as a vasodilation is the predicted response to fulfill the classical role of increasing oxygen and nutrients supply to active neurons. The SON is one of the most vascularized regions of the brain (Ambach and Palkovits, 1974; Badaut et al., 2000) with a dense capillary network resulting in a higher vascular-to-neuronal ratio than that needed to meet the expected metabolic demands of the neurons (Badaut et al., 2000). This suggests that the SON vasculature could serve a function beyond oxygen and nutrient delivery, including facilitation of readout of homeostatic variables, such as Na^+ or other osmolytes (Badaut et al., 2000). We show here that the inverse NVC response triggered by a systemic salt load generates a hypoxic, pro-excitatory milieu for VP neurons. This is supported by the observed reduction in blood flow and the increased tissue hypoxia, as demonstrated by an ~2.5-fold increase in HIF-1α mRNA. Moreover, we show that hypoxia, a stimulus that, in the cortex, can transiently suppress pyramidal neuronal firing (Dale and Frenguelli, 2009; van Aerde et al., 2015), leads to an increase in SON VP neuronal activity. Thus, we postulate that the inverse NVC triggered by the salt load forms part of a local positive-feedback mechanism that enables VP neurons to sustain high activity levels needed to reestablish ion and fluid homeostasis in the face of a persistent challenge.

Remarkably, VP neurons possess an unusually high tolerance to a hypoxic and hypoglycemic milieu compared to other neuronal types. SON neurons respond to oxygen- and oxygen-glucose deprivation with a transient depolarization and increase firing (Brisson and Andrew, 2012). Contrary to pyramidal neurons, SON neurons fully recover from the ischemic event (Brisson and Andrew, 2012). Moreover, compared to neocortical or other hypothalamic neuronal populations, SON neurons have a strong resilience to excitotoxicity (Herman and Wiegand, 1986; Hu et al., 1992) and severe ischemia as in stroke (Currás-Collazo et al., 2002). Thus, it is reasonable to speculate that the SON may employ the hypoxic pro-excitatory environment to enable the prolonged neuronal response needed to restore systemic homeostasis.

Dendritically released VP as the local vasoactive signal

Salt loading increases the systemic and local release of VP via axon terminals in the posterior pituitary gland and dendrites in SON and paraventricular nucleus (+PVN), respectively (Ludwig et al., 1994). Circulating VP has limited access across the blood-brain barrier, and if any, access is slow (Zlokovic et al., 1990). In addition, blockade of V1a receptors abolished the salt-load-induced vasoconstriction, thus supporting dendritic release of VP as the signal mediating the inverse NVC response. Moreover, the *in vivo* imaging of juxtaposed large vasopressin-enriched varicosities with parenchymal vessels in the SON supports an anatomical substrate for the local regulation of vascular tone via dendritically released VP.

Dendritic release of VP is activity dependent, involves Ca^{2+}-dependent exocytosis, and can occur independently from axonal release (Ludwig and Leng, 2006; Ludwig et al., 2002). Compared to the release of a conventional neurotransmitter, such as glutamate (millisecond range), a key signal triggering canonical NVC responses (Iadecola, 2017), the stimulus-evoked release of VP occurs at a slower timescale (minutes range; Ludwig and Leng, 2006;

Author Manuscript Author Manuscript Author Manuscript Author Manuscript

Pitra et al., 2019). Moreover, dendritically released VP diffuses across the extracellular space to act as a volume transmitter capable of affecting neighboring targets (Son et al., 2013). Thus, even though not directly tested in this study, we propose that the specificity of the inverse NVC reported here is largely determined by the extent to which dendritically released VP diffuses across the extracellular space (diffusion action radius estimated to be up to 120 μm; Chini et al., 2017) and the presence or absence of VP receptors at the target tissues (Son et al., 2013). Alternatively, possible mechanisms driving upstream- or distant-activity-induced constriction could be those underlain by conducted vasomotor responses initiated at the capillary (Dora et al., 2003; Longden et al., 2017). Thus, given the aforementioned properties and that VP is a potent peripheral vasoconstrictor, this peptide is ideal for mediating the salt-dependent inverse NVC response described here.

Blockade of V1a receptors unmasked an underlying salt-induced vasodilation. As with vasoconstrictions, these were also activity dependent, as they were blocked by TTX. Consistent with the kinetics of the inverse NVC response, the vasodilation was delayed and slow evolving. Thus, we speculate that, similar to NVC in other brain regions and in response to different stimuli (Lecrux et al., 2019), salt-induced VP neuron activity results in the simultaneous release of opposing vasoactive mediators, where the VP-mediated vasoconstriction has an early dominant effect. The slow buildup of a vasodilatory signal(s) may serve multiple functions, including dampening and/or terminating the VP-induced vasoconstriction as well as delivering oxygen and nutrients to metabolically active neurons. We previously showed in an *ex vivo* preparation that VP and nitric oxide might be part of this delicate vasoconstrictive and vasodilatory functional balance (Du et al., 2015). Although supported by *ex vivo* studies, the notion of a tight vasoconstriction-vasodilation dynamic signaling modality underlying homeostatic responses to a salt load has not been previously reported *in vivo*.

Concluding statement

Taken together, our data reveal the importance of brain region specificity and heterogeneity in NVC responses, such that the classical notion of NVC-mediated vasodilation to match energy supply to metabolic demand does not apply to all brain regions, which might impact the interpretation of blood-oxygen-level-dependent (BOLD) and functional magnetic resonance imaging (fMRI) in deep-brain structures. Using the regulation of body fluid balance by hypothalamic VP neurons as a model, we provide evidence for inverse NVC as a critical mechanism underpinning the role of the brain in the restoration of bodily homeostasis upon a systemic challenge. Specifically, we show that the activity-dependent, vasoconstriction-induced hypoxic milieu triggered a positive-feedback mechanism, which sustained the activity of VP neurons in response to an acute salt load.

STAR★METHODS

RESOURCE AVAILABILITY

Lead contact—Further information and requests for resources and reagents should be directed to and will be fulfilled by the Lead Contact, Prof. Javier E Stern (jstern@gsu.edu).

Author Manuscript Author Manuscript Author Manuscript Author Manuscript

Materials availability—This study did not generate new unique reagents.

Data and code availability—All data reported in this paper will be shared by the lead contact upon request. This paper does not report original code. Any additional information required to reanalyze the data reported in this paper is available from the lead contact upon request.

EXPERIMENTAL MODEL AND SUBJECT DETAILS

Animals—Male and female heterozygous transgenic eGFP-VP Wistar rats (Ueta et al., 2005) (250–490 g, 8–16 weeks old, n = 70) were used for all experiments. Rats were housed in cages (2 per cage) under constant temperature (22 ± 2°C) and humidity (55 ± 5%) on a 12-h light cycle (lights on: 08:00–20:00). All performed experiments were approved by the Georgia State University, Augusta University or University of Otago Institutional Animal Care and Use Committee (IACUC) and carried out in agreement with the IACUC guidelines. At all times, animals had *ad libitum* access to food and water and all efforts were made to minimize suffering and the numbers of animals used for the study.

METHOD DETAILS

Surgery for *in vivo* 2-photon imaging of the rat supraoptic nucleus—A transpharyngeal approach was used to expose the surface of the hypothalamus that was modified from that used to expose the SON (Brown et al. (2014); Ludwig and Leng, 1997). Briefly, rats were anesthetized by intraperitoneal injection of urethane (1.5 g/kg). Upon cessation of the hindlimb withdrawal reflex, the trachea was intubated, and the left femoral vein catheterized. The rat was then placed on a supine position on a heating pad on a stereotaxic frame (Stoelting 51600 Lab Standard Stereotaxic Instrument). After the oral cavity was opened by splitting the mandibles, cautery (Thermal Cautery Unit®, Geiger Medical Technologies, IA, USA) and drilling were used to remove the molars, ventromedial aspect of the right temporal bone, the basisphenoid and presphenoid bones to expose the ventral surface of the hypothalamus and ventral aspect of the right temporal lobe. The meninges overlying the right SON were removed and a stainless-steel ring (i.d. 3.6 mm) was placed on the surface of the brain with the junction of the posterior communicating artery and middle cerebral artery at the center.

In vivo 2-photon imaging of the SON

In vivo imaging of eGFP-VP neurons in the SON: The exposed ventral surface of the brain was covered with optical gel and the SON imaged under a 2-photon microscope (Bruker Ultima Investigator, Bruker, Billerica, MA) excited with a Ti:Sapphire laser (Chameleon Ultra II [Coherent, Santa Clara, CA]) tuned at 840 or 940 nm and scanned with resonant galvanometers through a 16X (numerical aperture 0.8) water immersion objective (Olympus, Center Valley, PA). Galvanometric scanning (for general imaging and time-lapse series) and resonant scanning (for imaging vessel dye loading and for RBC velocity) were controlled by PrairieView (Bruker, Billerica, MA) software.

In vivo imaging of the arterial and venous filling phases of the SON vasculature: The artery-specific dye Alexa Fluor 633 (Shen et al., 2012) (1–2 mg/kg), injected (i.v.) 1.5 h

Author Manuscript Author Manuscript Author Manuscript Author Manuscript

before 2-photon imaging recordings was used to label and differentiate SON arterioles from venules, Figure 1. Time-lapse imaging was performed using the resonant scanning mode at 30 Hz frame rate, 512 × 512 pixels during the intravenous administration of rhodamine or fluorescein 70 kDa dextrans (20 mg/ml, 200 nl/rat).

In vivo vessel diameter quantification: Salt loading was performed via the femoral vein catheter by graded infusion of HTS (1 mL of 2 M NaCl over 30 min) or isotonic saline (1 mL of 0.15 M NaCl), the latter used as control. V1a receptor antagonist (β-mercapto-β,β-cyclopenta methylene propionyl) (Sigma-Aldrich, St Louis, MO) and Tetrodotoxin (TTX) (Alomone Labs, Jerusalem, Israel) were dissolved in the optical gel before application (at least 30 mins before the onset of IV infusions). To quantify changes in vessel diameter during the HTS, a time-series, Z stack acquisition protocol was used (1 iteration: 20 images at 0.33 Hz 30 μm interval up/down the Z axis in the SON; a total of 20 iterations with a 120 s interval; 512 × 512 pixels).

An inherent limitation of our approach was the presence of low frequency (~1.0 Hz) oscillations/pulsations. During imaging acquisitions, pulsations manifested as oscillations in the intensity signal of the vascular labeling. We compared the diameters of a subset of control vessels in the “down” and “up” phases of the intensity profile and found that the vessel diameter was not different between the two phases (Figure S6), indicating that vessel diameter measurements were unaffected by the presence of mechanical pulsations.

The HTS stimulation started at iteration number 4. Analyses were performed with ImageJ. Briefly, a Z-projected image was obtained for each of the 20 iterations. To quantify diameter changes, a line was manually drawn along the cross-sectional axis of the vessel wall. A profile of image brightness was then obtained. The high contrast between the vessel wall and brain parenchyma allows for the ready detection of the vessel wall edges, which appeared as a sudden rise in basal fluorescence. The distance between the two fast-rising phases, measured just above the base of the fluorescence profile, was used to measure diameter changes over time. Plots of diameter changes were obtained to address the vascular response to the stimulus (e.g., hypertonic challenge), see examples in Figures 2 and S7. To validate our approach, we tested the effects of acetylcholine (ACh), a well-established signal leading to endothelial-mediated vasodilation (Domeier and Segal, 2007; Emerson and Segal, 2000). Consistent with observations from other vascular beds, ACh (10 μM, 250 μl i.v.) significantly dilated SON arterioles (one-way repeated-measures (RM) ANOVA, $p = 0.0001$ $n = 12$ vessels from 4 rats, Figure S7).

In vivo blood velocity quantification: Blood velocity was calculated by monitoring the movement of red blood cells (RBC, which appeared as moving dark spots in fluorescently-labeled vessels) through a segment of an imaged vessel during the time course of the HTS challenge. To this end, a separate set of experiments were performed, in which high-speed (500–1000 Hz, 5–10 s) resonant scanning images were obtained from a small region of interest (on average 150 × 25 pixels) drawn across the width of the vessel of interest. This procedure was repeated in multiple iterations (240 s interval) throughout the hypertonic challenge. For analysis of velocity, kymographs were constructed in ImageJ by drawing a line along the longitudinal axis of the vessel. In these graphs, the movement of RBCs

Author Manuscript Author Manuscript Author Manuscript Author Manuscript

appears as streaks in space-time images, in which the streak angle is a function of the RBC velocity (Chhatbar and Kara, 2013). A representative kymograph and bar graphs summarizing mean basal velocities obtained from ICAs, arterioles and venules is shown in Figure S1.

Collection of cerebrospinal fluid (CSF) and plasma for osmolarity measurements—Rats were deeply anesthetized with an intraperitoneal injection of urethane (1.5 g/kg). At the end of an isotonic or HTS infusion (i.v.), as described above, the skin of the back of the head and neck were shaved, and a vertical midline incision was made from the occiput toward the neck to expose the cisterna magna. A 27-gauge needle was inserted into the cisterna magna and negative pressure was applied to extract CSF. Blood was collected and plasma separated via centrifugation (2200–2500 RPM). Osmolarity of the freshly obtained CSF and plasma were measured using a micro osmometer (Advanced Instruments, Model-3300, Version-4.3, Massachusetts, USA).

Cardiovascular endpoints and blood gas measurements—The left femoral artery and vein were catheterized for blood pressure (BP) and heart rate (HR) measurements, and delivery of saline solutions, respectively. The distal end of the artery catheter filled with heparinized fluid (20IU/ml) was connected to a calibrated pressure transducer with disposable clip-on BP domes (model SP844, Memscap AS, Norway) coupled to an amplifier and recording device (Bridge 40Amp/PowerLab 4/35, ADInstruments, Australia). Data were collected throughout of the 30 min saline injections and analyzed with the blood pressure module for LabChart 8 software and plotted for statistical analyses (GraphPad Prism 8, USA). At the end of the experiment, a sample of arterial blood (0.5 ml) was collected for blood gas analyses (ABG, Stat Profile, pHOz Ultra, Nova Biomedical, USA).

Electrophysiological recording from brain slices—Hypothalamic slices containing the SON were obtained as previously described (Stern, 2001). Following anesthesia with pentobarbital (50 mg/kg), rats were perfused through the heart with a cold sucrose solution (containing in mM: 200 sucrose, 2.5 KCl, 3 $MgSO_4$, 26 $NaHCO_3$, 1.25 NaH_2PO_4, 20 D-glucose, 0.4 ascorbic acid, 1 $CaCl_2$ and 2 pyruvic acid (290–310 mosmol l^{-1}). Rat brains were then removed and coronal slices (300 μm) obtained in ice-cold aCSF (containing in mM: 119 NaCl, 2.5 KCl, 1 $MgSO_4$, 26 $NaHCO_3$, 1.25 NaH_2PO_4, 20 D-glucose, 0.4 ascorbic acid, 2 $CaCl_2$ and 2 pyruvic acid; pH 7.4; 290–310 mosmol/l) gassed with 95% O_2-5% CO_2, using a vibroslicer (Leica VT1200s, Leica Microsystems). Slices were kept in a gassed aCSF chamber at room temperature until used. In the recording chamber, slices were bathed with aCSF (~3.0 ml/min) continuously gassed with 95% O_2-5% CO_2 and maintained at ~32°C. Conventional whole-cell patch-clamp recordings were obtained as previously described (Stern, 2001). Patch pipettes (4–7 MΩ) composed of thin-walled (1.5 mm outer diameter, 1.17 mm inner diameter) borosilicate glass (GC150T-7.5, Clark, Reading, UK), were pulled on a horizontal electrode puller (P-97, Sutter Instruments, Novato, CA). The internal solution contained (in mM): 135 potassium gluconate, 0.2 EGTA, 10 HEPES, 10 KCl, 0.9 $MgCl_2$, 4 MgATP, 0.3 NaGTP and 20 phosphocreatine (Na^+); pH 7.2–7.3. Recordings were obtained with a Multiclamp 700A amplifier (Axon Instruments, Foster City, Ca) using infrared differential interference contrast (IR-DIC) video microscopy.

Author Manuscript Author Manuscript Author Manuscript Author Manuscript

The voltage-output was digitized at 16-bit resolution, 10 kHz (Digidata 1320A, Axon Instruments), and saved on a computer for offline analysis. For current-clamp recordings, protocols included an output gain of 10 and a Bessel filter of 10 kHz. Spontaneous firing activity was recorded in continuous mode before, during and after bath application of 20% O_2. Mean firing frequency over time was generated using Mini Analysis software (Synaptosoft Inc., NJ).

***In vivo* electrophysiology—**Rats were anesthetized with urethane (1.50 g/kg) for extracellular single-unit recording of spike firing. Upon cessation of the flexor withdrawal reflex, the left femoral vein was catheterized for hypertonic saline infusion as previously described. A rat was placed supine on a stereotaxic frame and the right SON exposed through the oral and nasal cavities Brown et al. (2014). Extracellular single-unit recordings were made via a glass recording microelectrode filled with 0.9% saline (placed through the loop of the microdialysis probe), using a Neurolog system connected to a CED 1401 analog-digital interface (Cambridge Electronic Design) and Spike 2 software (Cambridge Electronic Design). Antidromic spikes were evoked in vasopressin neurons prior to recording using a side-by-side SNEX-200 stimulating electrode (Science Products GmbH) placed on the pituitary stalk. Vasopressin neurons were differentiated from neighboring oxytocin neurons by the lack of excitation in response to (Tyr[SO_3H]^{27}) Cholecystokinin fragment 26–33 amide (20 μg/kg) (Sigma-Aldrich, St Louis, MO) (Scott et al., 2009).

Measurement of tissue partial pressure of oxygen (pO_2)—Partial pressure of tissue O_2 (pO_2) in the SON was recorded using an optical fluorescence probe (250 μm tip diameter; OxyLite system; Oxford Optronix) that allows real-time recording of absolute changes in tissue pO_2. Rats were anesthetized with urethane (1.5 g/kg) and the SON exposed as described above. Rats were positioned in a stereotaxic apparatus, and the SON exposed using a transpharyngeal surgery as described above. For these experiments, and to obtain a stable baseline pO_2, rats were mechanically ventilated using a positive pressure ventilator with a tidal volume of ~1 mL per 100 g of body weight and a frequency of 85 strokes min^{-1}. The sensor was placed 1–2 mm below the ventral surface of the brain, medially to the bifurcation of the ICA and the MCA (Figure 1). The sensor was then retracted ~0.1 mm to its final position to reduce compression of the tissue and allowed to equilibrate for at least 15–20 minutes. SON pO_2 was recorded at baseline and during the HTS infusion at a rate of 1 Hz. To further validate the sensitivity of the sensor, measurements were recorded in response to 100% O_2 breathing as well as a transient partial occlusion of the tracheal cannula (Figures S5C and S5D).

Reverse transcription-polymerase chain reaction (RT-PCR) and quantitative real-time PCR (qPCR).—RNA isolation was performed using the miRNAeasy Mini kit (QIAGEN, Cat. No. 217004) and the QIAzol Lysis Reagent (QIAGEN, Cat. No. 1023537) with 250 μm-thick tissue punches (1 mm diameter) per the manufacturer's protocol. SON punches (8 per animal), were collected from Bregma −0.7 mm to −1.7 mm. After measuring the RNA concentration using NanoDrop One (Thermo Scientific), cDNA synthesis was performed using the iScript™ gDNA Clear cDNA Synthesis Kit (BIO RAD, cat. no. 1725035) and the SimpliAmp Thermal Cycler (applied biosystems,

Author Manuscript Author Manuscript Author Manuscript Author Manuscript

Thermo Fisher Scientific) following the manufacturer's protocol. qPCR was conducted using the following 10x QuantiTect primers (diluted in 1.1 mL TE ph 8.0) purchased from QIAGEN: Beta-actin (rat): QT01830458 and HIF-1α (rat): QT00193473. All individual qPCR reactions were triplicated and averaged for statistical analysis. Data analysis was performed using the LightCycler96 software from Roche using the relative normalized ratio of the qPCR reactions versus the respective beta-actin controls. This approach was used to quantitatively assess changes in HIF-1α mRNA in rats exposed either to an isotonic (0.15 M) or hypertonic (2 M) saline infusion (1 ml, 30 over 30 min), or following a 30 min partial occlusion of the ICA, just caudal to the branching point of the MCA (Proline 6–0 suture, Ethicon, 8805H, USA). In all cases, brains were dissected and snap-frozen immediately after the occlusion. Brains were then processed as described above.

QUANTIFICATION AND STATISTICAL ANALYSIS

Statistical analyses were performed using Prism 8 (GraphPad, CA, USA). Quantitative data were expressed as the MEAN ± SEM. No statistical methods were used to predetermine sample sizes, but sample sizes in the current study were similar to our previous reports (Althammer et al., 2020; Leng et al., 2001; Son et al., 2013). Rats were randomly allocated to groups in all experiments. Data collection and analyses were not performed blindly to the conditions of the experiments. Data were analyzed by paired or unpaired t test (two-sided in all cases) or one-way repeated-measures (RM) analysis of variance (ANOVA) with the post hoc Bonferroni's multiple comparisons test. For qPCR analysis of fold changes in expression, a one-sample t test against the hypothetical mean ± 1 was used (Althammer et al., 2020). Data distribution was assumed to be normal, although this was not formally tested. Values were considered significantly different at $p < 0.05$. Statistical details of experiments can be found in the figure legends.

Supplementary Material

Refer to Web version on PubMed Central for supplementary material.

ACKNOWLEDGMENTS

Grant support was provided by (to J.E.S.) National Institute of Neurological Disorders and Stroke (NINDS) grant NIH R01NS094640, (to J.A.F.) NIH NINDS 1R01NS082521–01, (to C.H.B.) Royal Society Te Aparangi Marsden Fund contract no. UOO1602, and (to F.A.) DFG Postdoc Fellowship AL 2466/1–1. We acknowledge S.C. Peaden, C. Weaver, and S. Byron for their contribution to the cardiovascular and gas blood measurements.

REFERENCES

Acer N, Sahin B, Usanmaz M, Tatoğlu H, and Irmak Z (2008). Comparison of point counting and planimetry methods for the assessment of cerebellar volume in human using magnetic resonance imaging: a stereological study. Surg. Radiol. Anat. 30, 335–339. [PubMed: 18292960]

Althammer F, Ferreira-Neto HC, Rubaharan M, Roy RK, Patel AA, Murphy A, Cox DN, and Stern JE (2020). Three-dimensional morphometric analysis reveals time-dependent structural changes in microglia and astrocytes in the central amygdala and hypothalamic paraventricular nucleus of heart failure rats. J. Neuroinflammation 17, 221. [PubMed: 32703230]

Ambach G, and Palkovits M (1974). Blood supply of the rat hypothalamus. II. Nucleus paraventricularis. Acta Morphol. Acad. Sci. Hung. 22, 311–320. [PubMed: 4467690]

Author Manuscript Author Manuscript Author Manuscript Author Manuscript

Ambach G, and Palkovits M (1979). The blood supply of the hypothalamus in the rat. In Handbook of the Hypothalamus, Morgane PJ and Panksepp J, eds. (Dekker M), pp. 267–377.

Badaut J, Nehlig A, Verbavatz J, Stoeckel M, Freund-Mercier MJ, and Lasbennes F (2000). Hypervascularization in the magnocellular nuclei of the rat hypothalamus: relationship with the distribution of aquaporin-4 and markers of energy metabolism. J. Neuroendocrinol. 12, 960–969. [PubMed: 11012836]

Balbi M, Koide M, Wellman GC, and Plesnila N (2017). Inversion of neurovascular coupling after subarachnoid hemorrhage in vivo. J. Cereb. Blood Flow Metab. 37, 3625–3634. [PubMed: 28112024]

Bere Z, Obrenovitch TP, Bari F, and Farkas E (2014). Ischemia-induced depolarizations and associated hemodynamic responses in incomplete global forebrain ischemia in rats. Neuroscience 260, 217–226. [PubMed: 24365459]

Bourque CW (2008). Central mechanisms of osmosensation and systemic osmoregulation. Nat. Rev. Neurosci. 9, 519–531. [PubMed: 18509340]

Bourque CW, Ciura S, Trudel E, Stachniak TJ, and Sharif-Naeini R (2007). Neurophysiological characterization of mammalian osmosensitive neurones. Exp. Physiol. 92, 499–505. [PubMed: 17350993]

Brisson CD, and Andrew RD (2012). A neuronal population in hypothalamus that dramatically resists acute ischemic injury compared to neocortex. J. Neurophysiol. 108, 419–430. [PubMed: 22514289]

Brown C, Han S, Moaddab M, Scott V, and Schwenke D (2014). Peptidergic control of oxytocin and vasopressin neurons and its role in reproductive and hypertension-associated plasticity. In Neurophysiology of Neuroendocrine Neurons, Armstrong WE and Tasker JG, eds. (Wiley-Blackwell), pp. 65–86.

Brown CH, Ludwig M, Tasker JG, and Stern JE (2020). Somato-dendritic vasopressin and oxytocin secretion in endocrine and autonomic regulation. J. Neuroendocrinol. 32, e12856. [PubMed: 32406599]

Cai C, Fordsmann JC, Jensen SH, Gesslein B, Lønstrup M, Hald BO, Zambach SA, Brodin B, and Lauritzen MJ (2018). Stimulation-induced increases in cerebral blood flow and local capillary vasoconstriction depend on conducted vascular responses. Proc. Natl. Acad. Sci. USA 115, E5796–E5804. [PubMed: 29866853]

Cauli B, and Hamel E (2010). Revisiting the role of neurons in neurovascular coupling. Front. Neuroenergetics 2, 9. [PubMed: 20616884]

Cauli B, Tong XK, Rancillac A, Serluca N, Lambolez B, Rossier J, and Hamel E (2004). Cortical GABA interneurons in neurovascular coupling: relays for subcortical vasoactive pathways. J. Neurosci. 24, 8940–8949. [PubMed: 15483113]

Chhatbar PY, and Kara P (2013). Improved blood velocity measurements with a hybrid image filtering and iterative Radon transform algorithm. Front. Neurosci. 7, 106. [PubMed: 23807877]

Chini B, Verhage M, and Grinevich V (2017). The action radius of oxytocin release in the mammalian CNS: from single vesicles to behavior. Trends Pharmacol. Sci. 38, 982–991. [PubMed: 28899620]

Choudhry H, and Harris AL (2018). Advances in hypoxia-inducible factor biology. Cell Metab. 27, 281–298. [PubMed: 29129785]

Currás-Collazo MC, Patel UB, and Hussein MO (2002). Reduced susceptibility of magnocellular neuroendocrine nuclei of the rat hypothalamus to transient focal ischemia produced by middle cerebral artery occlusion. Exp. Neurol. 178, 268–279. [PubMed: 12504885]

Dale N, and Frenguelli BG (2009). Release of adenosine and ATP during ischemia and epilepsy. Curr. Neuropharmacol. 7, 160–179. [PubMed: 20190959]

de la Torre JC (1976). Evidence for central innervation of intracerebral blood vessels: local cerebral blood flow measurements and histofluorescence analysis by the sucrose-phosphate-glyoxylic acid (SPG) method. Neuroscience 1, 455–457. [PubMed: 11370237]

Devonshire IM, Papadakis NG, Port M, Berwick J, Kennerley AJ, Mayhew JE, and Overton PG (2012). Neurovascular coupling is brain region-dependent. Neuroimage 59, 1997–2006. [PubMed: 21982928]

Author Manuscript Author Manuscript Author Manuscript Author Manuscript

Devor A, Tian P, Nishimura N, Teng IC, Hillman EM, Narayanan SN, Ulbert I, Boas DA, Kleinfeld D, and Dale AM (2007). Suppressed neuronal activity and concurrent arteriolar vasoconstriction may explain negative blood oxygenation level-dependent signal. J. Neurosci. 27, 4452–4459. [PubMed: 17442830]

Devor A, Hillman EM, Tian P, Waeber C, Teng IC, Ruvinskaya L, Shalinsky MH, Zhu H, Haslinger RH, Narayanan SN, et al. (2008). Stimulus-induced changes in blood flow and 2-deoxyglucose uptake dissociate in ipsilateral somatosensory cortex. J. Neurosci. 28, 14347–14357. [PubMed: 19118167]

Domeier TL, and Segal SS (2007). Electromechanical and pharmacomechanical signalling pathways for conducted vasodilatation along endothelium of hamster feed arteries. J. Physiol. 579, 175–186. [PubMed: 17138602]

Dora KA, Xia J, and Duling BR (2003). Endothelial cell signaling during conducted vasomotor responses. Am. J. Physiol. Heart Circ. Physiol. 285, H119–H126. [PubMed: 12793976]

Du W, Stern JE, and Filosa JA (2015). Neuronal-derived nitric oxide and somatodendritically released vasopressin regulate neurovascular coupling in the rat hypothalamic supraoptic nucleus. J. Neurosci. 35, 5330–5341. [PubMed: 25834057]

Emerson GG, and Segal SS (2000). Endothelial cell pathway for conduction of hyperpolarization and vasodilation along hamster feed artery. Circ. Res. 86, 94–100. [PubMed: 10625310]

Gouzènes L, Desarménien MG, Hussy N, Richard P, and Moos FC (1998). Vasopressin regularizes the phasic firing pattern of rat hypothalamic magnocellular vasopressin neurons. J. Neurosci. 18, 1879–1885. [PubMed: 9465012]

Haam J, Halmos KC, Di S, and Tasker JG (2014). Nutritional state-dependent ghrelin activation of vasopressin neurons via retrograde transneuronal-glial stimulation of excitatory GABA circuits. J. Neurosci. 34, 6201–6213. [PubMed: 24790191]

Hatton GI (1997). Function-related plasticity in hypothalamus. Annu. Rev. Neurosci. 20, 375–397. [PubMed: 9056719]

Herman JP, and Wiegand SJ (1986). Ibotenate-induced cell death in the hypothalamic paraventricular nucleus: differential susceptibility of magnocellular and parvicellular neurons. Brain Res. 383, 367–372. [PubMed: 3768702]

Hinzman JM, Andaluz N, Shutter LA, Okonkwo DO, Pahl C, Strong AJ, Dreier JP, and Hartings JA (2014). Inverse neurovascular coupling to cortical spreading depolarizations in severe brain trauma. Brain 137, 2960–2972. [PubMed: 25154387]

Hu B, Cunningham JT, Nissen R, Renaud LP, and Bourque CW (1992). Rat supraoptic neurons are resistant to glutamate neurotoxicity. Neuroreport 3, 87–90. [PubMed: 1351757]

Iadecola C (2017). The neurovascular unit coming of age: a journey through neurovascular coupling in health and disease. Neuron 96, 17–42. [PubMed: 28957666]

Lecrux C, Bourourou M, and Hamel E (2019). How reliable is cerebral blood flow to map changes in neuronal activity? Auton. Neurosci. 217, 71–79. [PubMed: 30744905]

Leng G, Brown CH, Bull PM, Brown D, Scullion S, Currie J, Blackburn-Munro RE, Feng J, Onaka T, Verbalis JG, et al. (2001). Responses of magnocellular neurons to osmotic stimulation involves coactivation of excitatory and inhibitory input: an experimental and theoretical analysis. J. Neurosci. 21, 6967–6977. [PubMed: 11517284]

Leng G, Brown C, Sabatier N, and Scott V (2008). Population dynamics in vasopressin cells. Neuroendocrinology 88, 160–172. [PubMed: 18667805]

Li N, Jia X, Murari K, Parlapalli R, Rege A, and Thakor NV (2009). High spatiotemporal resolution imaging of the neurovascular response to electrical stimulation of rat peripheral trigeminal nerve as revealed by in vivo temporal laser speckle contrast. J. Neurosci. Methods 176, 230–236. [PubMed: 18706442]

Longden TA, Dabertrand F, Koide M, Gonzales AL, Tykocki NR, Brayden JE, Hill-Eubanks D, and Nelson MT (2017). Capillary K^+-sensing initiates retrograde hyperpolarization to increase local cerebral blood flow. Nat. Neurosci. 20, 717–726. [PubMed: 28319610]

Ludwig M, and Leng G (1997). Autoinhibition of supraoptic nucleus vasopressin neurons *in vivo*: a combined retrodialysis/electrophysiological study in rats. Eur. J. Neurosci. 9, 2532–2540. [PubMed: 9517458]

Author Manuscript Author Manuscript Author Manuscript Author Manuscript

Ludwig M, and Leng G (2006). Dendritic peptide release and peptide-dependent behaviours. Nat. Rev. Neurosci. 7, 126–136. [PubMed: 16429122]

Ludwig M, Callahan MF, Neumann I, Landgraf R, and Morris M (1994). Systemic osmotic stimulation increases vasopressin and oxytocin release within the supraoptic nucleus. J. Neuroendocrinol. 6, 369–373. [PubMed: 7987366]

Ludwig M, Sabatier N, Bull PM, Landgraf R, Dayanithi G, and Leng G (2002). Intracellular calcium stores regulate activity-dependent neuropeptide release from dendrites. Nature 418, 85–89. [PubMed: 12097911]

Perrenoud Q, Rossier J, Férézou I, Geoffroy H, Gallopin T, Vitalis T, and Rancillac A (2012). Activation of cortical 5-HT(3) receptor-expressing interneurons induces NO mediated vasodilatations and NPY mediated vasoconstrictions. Front. Neural Circuits 6, 50. [PubMed: 22907992]

Pitra S, Zhang M, Cauley E, and Stern JE (2019). NMDA receptors potentiate activity-dependent dendritic release of neuropeptides from hypothalamic neurons. J. Physiol. 597, 1735–1756. [PubMed: 30629746]

Scott V, Bishop VR, Leng G, and Brown CH (2009). Dehydration-induced modulation of kappa-opioid inhibition of vasopressin neurone activity. J. Physiol. 587, 5679–5689. [PubMed: 19822541]

Shen Z, Lu Z, Chhatbar PY, O'Herron P, and Kara P (2012). An artery-specific fluorescent dye for studying neurovascular coupling. Nat. Methods 9, 273–276. [PubMed: 22266543]

Silva AC, Lee SP, Iadecola C, and Kim SG (2000). Early temporal characteristics of cerebral blood flow and deoxyhemoglobin changes during somatosensory stimulation. J. Cereb. Blood Flow Metab. 20, 201–206. [PubMed: 10616809]

Son SJ, Filosa JA, Potapenko ES, Biancardi VC, Zheng H, Patel KP, Tobin VA, Ludwig M, and Stern JE (2013). Dendritic peptide release mediates interpopulation crosstalk between neurosecretory and preautonomic networks. Neuron 78, 1036–1049. [PubMed: 23791197]

Stern JE (2001). Electrophysiological and morphological properties of preautonomic neurones in the rat hypothalamic paraventricular nucleus. J. Physiol. 537, 161–177. [PubMed: 11711570]

Tian P, Teng IC, May LD, Kurz R, Lu K, Scadeng M, Hillman EM, De Crespigny AJ, D'Arceuil HE, Mandeville JB, et al. (2010). Cortical depth-specific microvascular dilation underlies laminar differences in blood oxygenation level-dependent functional MRI signal. Proc. Natl. Acad. Sci. USA 107, 15246–15251. [PubMed: 20696904]

Ueta Y, Fujihara H, Serino R, Dayanithi G, Ozawa H, Matsuda K, Kawata M, Yamada J, Ueno S, Fukuda A, and Murphy D (2005). Transgenic expression of enhanced green fluorescent protein enables direct visualization for physiological studies of vasopressin neurons and isolated nerve terminals of the rat. Endocrinology 146, 406–413. [PubMed: 15375027]

Uhlirova H, Kılıç, K, Tian P, Thunemann M, Desjardins M, Saisan PA, Sakadžić S, Ness TV, Mateo C, Cheng Q, et al. (2016). Cell type specificity of neurovascular coupling in cerebral cortex. eLife 5, e14315. [PubMed: 27244241]

Urban A, Golgher L, Brunner C, Gdalyahu A, Har-Gil H, Kain D, Montaldo G, Sironi L, and Blinder P (2017). Understanding the neurovascular unit at multiple scales: advantages and limitations of multi-photon and functional ultrasound imaging. Adv. Drug Deliv. Rev. 119, 73–100. [PubMed: 28778714]

van Aerde KI, Qi G, and Feldmeyer D (2015). Cell type-specific effects of adenosine on cortical neurons. Cereb. Cortex 25, 772–787. [PubMed: 24108800]

Vázquez-Rodríguez B, Suárez LE, Markello RD, Shafiei G, Paquola C, Hagmann P, van den Heuvel MP, Bernhardt BC, Spreng RN, and Misic B (2019). Gradients of structure-function tethering across neocortex. Proc. Natl. Acad. Sci. USA 116, 21219–21227. [PubMed: 31570622]

Verbalis JG (2003). Disorders of body water homeostasis. Best Pract. Res. Clin. Endocrinol. Metab. 17, 471–503. [PubMed: 14687585]

Weber B, Keller AL, Reichold J, and Logothetis NK (2008). The microvascular system of the striate and extrastriate visual cortex of the macaque. Cereb. Cortex 18, 2318–2330. [PubMed: 18222935]

Yosten GL, and Samson WK (2012). Pressor doses of vasopressin result in only transient elevations in plasma peptide levels. Peptides 33, 342–345. [PubMed: 22227112]

Author Manuscript Author Manuscript Author Manuscript Author Manuscript

Zlokovic BV, Hyman S, McComb JG, Lipovac MN, Tang G, and Davson H (1990). Kinetics of arginine-vasopressin uptake at the blood-brain barrier. Biochim. Biophys. Acta 1025, 191–198. [PubMed: 2364078]

Author Manuscript Author Manuscript Author Manuscript Author Manuscript

Highlights

- Salt loading evokes activity-dependent vasoconstrictions in the SON
- Activity-dependent vasoconstrictions are mediated by dendritically released VP
- Vasoconstrictions reduce blood flow and generate a local hypoxia microenvironment
- Salt-loading vasoconstrictions evoke positive feedback excitation of VP neurons

Author Manuscript Author Manuscript Author Manuscript Author Manuscript

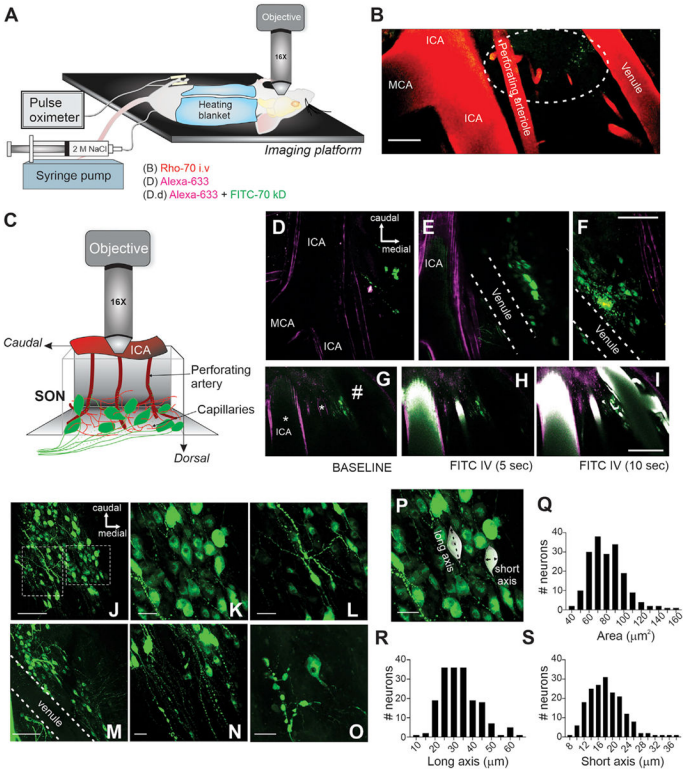

Figure 1. In two-photon imaging of the SON microvasculature

(A) Schematic representation of the *in vivo* preparation used.

(B) Low-magnification (16×) two-photon image of the visually accessible area of the SON depicting main vessels following rhodamine 70 kDa administration (i.v.). The dashed line oval shows the location of the SON with corresponding EGFP-VP-positive neurons (green), medially to the bifurcation of the ICA and the MCA. Note that the dense capillary network around SON neurons is not visible at this magnification and z plane.

(C) Simplified cartoon displaying the neurovascular cytoarchitecture of the SON. Highlighted is the internal carotid (ICA), a superficial pial artery from which perforating arterioles “dive” into the SON to give rise to a highly dense capillary network intimately associated with VP neurons (green, highlighting the EGFP-VP neurons).

(D–F) Starting at the surface (D) and down the z axis (E and F), representative two-photon images of the SON 1.5 h after i.v. injection of the artery-specific dye Alexa Fluor 633 (magenta). Note the evident Alexa 633 staining in the ICA, MCA, and perforating arterioles and lack of staining in the venule. EGFP-VP neurons are shown in green.

(G–I) *In vivo* time-lapse imaging of the SON vasculature-filling phase during the i.v. administration of fluorescein 70 kDa dextrans in Alexa Fluor 633 pre-labeled arterioles (*) and non-labeled (#) vessels. Note the delayed filling in the venule compared to the Alexa-Fluor-633-stained arterioles. ICA, internal carotid artery; MCA, middle cerebral artery.

(J–L) Images (J) of EGFP-VP-positive neurons in the SON shown at low magnification (16×). The right and left dashed squared areas are shown at higher magnification in (K) and (L), respectively.

(M) Image of EGFP-VP-positive neurons near a large venule running through the SON.

(N and O) Samples of varicose VP neuronal processes within the SON.

Author Manuscript Author Manuscript Author Manuscript Author Manuscript

(P) Image showing the long and short axes of EGFP-VP-positive neurons from where measurements were made.
(Q–S) Distribution histograms of the EGFP neuronal area (μm^2) and long and short axes (μm), respectively. A total of 181 EGFP-VP neurons were sampled.
(E) Starting at the surface (Ea) and down the z axis (Eb and Ec), two-photon images of the SON 1.5 h after i.v. injection of the artery-specific dye Alexa Fluor 633 (magenta). Note the evident Alexa Fluor 633 staining in the ICA, MCA, and perforating arterioles and lack of staining in the venule. EGFP-VP neurons are shown in scale bars: (B) 75 μm; (F) 200 μm; (I) 250 μm; (J–O) 50 μm; and (P) 50 μm.

Author Manuscript Author Manuscript Author Manuscript Author Manuscript

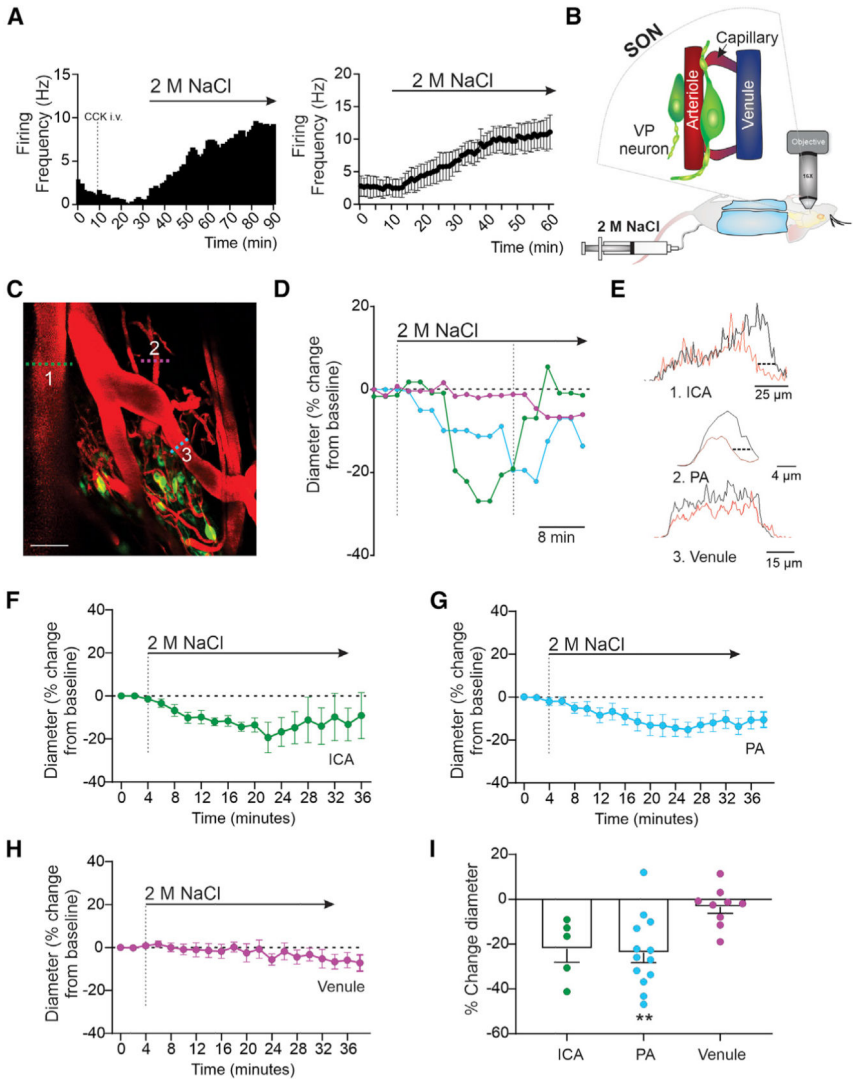

Figure 2. An acute salt load increases the firing activity of vasopressin neurons and induces vasoconstriction of SON arterioles

(A) *In vivo* recordings of antidromically identified VP neurons showing an increase in firing activity during a 2 M NaCl infusion (i.v.; 1 mL; 30 min). Left panel: representative example from an individual neuron is shown; right panel: averaged response is shown (n = 4; F = 18.8; $p < 0.0001$). Tyr[SO_3H][27]) cholecystokinin fragment 26–33 amide (CCK) was injected i.v. at the time indicated in the graph. The lack of response to CCK was used to identify the recorded cell as VP (Scott et al., 2009).

(B) Schematic representation of the *in vivo* preparation used for the imaging data shown in this figure.

(C) Low-magnification *in vivo* two-photon image of the SON following rhodamine 70 kDa administration (i.v.). The ICA (1), a PA (2), and a venule (3) are shown. EGFP-VP neurons are shown in green; dashed lines show the vessel segment from where diameter measurements were obtained.

Author Manuscript Author Manuscript Author Manuscript Author Manuscript

(D) Mean percent change in vessel diameter as a function of time during the HTS infusion. Vertical dashed lines correspond to the time period from where diameter measurements were extracted.

(E) Profiles of image brightness along the cross-section line of the vessels shown in (A) before (black) and during (red) HTS infusion. The dashed lines represent the change in diameter following NaCl stimulation.

(F–H) Mean vessel diameter changes as a function of time during HTS infusion in ICA ($n = 5$; $F = 1.76$; $p < 0.05$), PA ($n = 13$; $F = 3.60$; $p < 0.0001$), and venules ($n = 9$; $F = 0.76$; $p = 0.75$), respectively.

(I) Summary of mean delta peak diameter during the HTS infusion.

PA, perforating arteriole. **$p < 0.01$ versus venules, Bonferroni's post hoc test ($t = 3.44$). Scale bar: (C) 100 μm. Error bars represent SEM.

Author Manuscript Author Manuscript Author Manuscript Author Manuscript

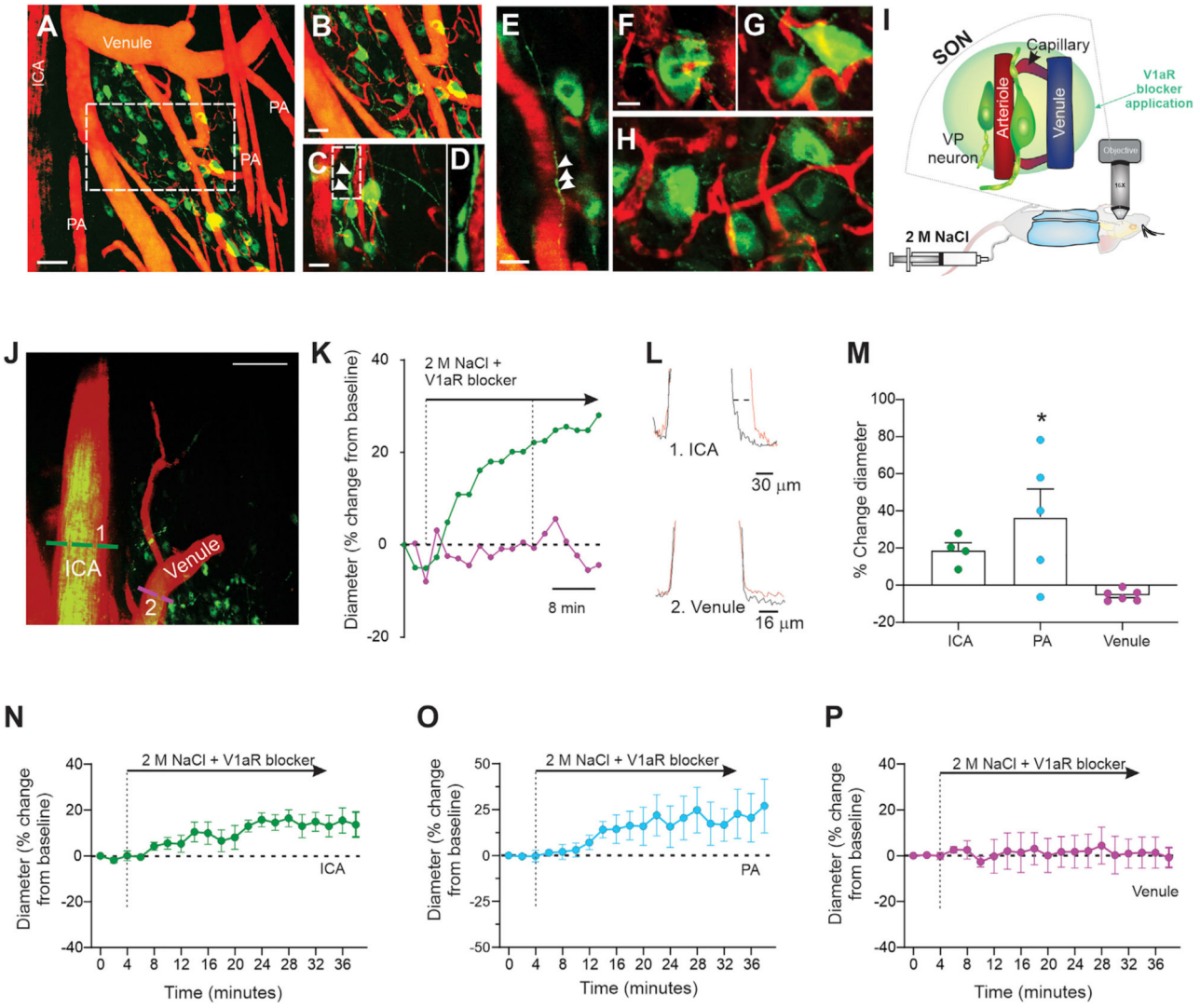

Figure 3. Salt-induced vasoconstrictions in the SON are blocked by topical application of a V1a receptor antagonist

(A) *In vivo* two-photon, high-resolution imaging of EGFP-VP neurons and the labeled SON microvasculature (rhodamine 70 kDa) underscoring the intimate association between these two key elements of the neurovascular unit.

(B) A higher magnification of the area within the dashed rectangle shown in (A).

(C) Image showing EGFP-VP neurons and thick dendritic varicosities juxtaposed to blood vessels (arrowheads).

(D) The rectangular area in (C) is shown at higher magnification.

(E) Image showing EGFP-VP varicose process (arrowheads) running along a stained blood vessel within the SON region,

(F–H) Images showing EGFP-VP neurons enwrapped by labeled capillaries.

(I) Schematic representation of the in vivo preparation used for the data shown in this figure.

(J) Low magnification of an *in vivo* two-photon image of the SON following rhodamine 70 kDa and fluorescein isothiocyanate (FITC) 70 kDa administration (i.v.). An ICA (1) and a

Author Manuscript Author Manuscript Author Manuscript Author Manuscript

venule (2) are shown. EGFP-VP neurons are shown in green; dashed lines show the vessel segment from where diameter measurements, shown in (K) and (L), were made.

(K) Summary plot of the percent change in vessel diameter as a function of time during HTS infusion (i.v.; 1 mL; 30 min) in the presence of a V1a receptor antagonist topically applied to the SON. Vertical dashed lines correspond to the time period from where diameter measurements were extracted.

(L) Profiles of image brightness along the cross-section line of the vessels shown in (C) before (black) and during (red) HTS infusion. The dashed lines represent the change in diameter following HTS stimulation.

(M) Summary of mean delta peak diameter during the HTS in the presence of the V1a receptor antagonist.

(N–P) Plots of mean vessel diameter changes as a function of time during HTS infusion in the presence of the V1a receptor antagonist in ICA ($n = 4$; $F = 5.74$; $p < 0.0001$), PA ($n = 5$; $F = 1.51$; $p = 0.107$), and venules ($n = 7$; $F = 0.21$; $p = 0.99$), respectively.

**$p < 0.01$ versus venules, Bonferroni's post hoc test ($t = 3.48$). Scale bars: (A) 100 μm; (B) 50 μm; (C) 30 μm; (E) 25 μm; (F) 12 μm; (J) 120 μm. Error bars represent SEM.

Author Manuscript Author Manuscript Author Manuscript Author Manuscript

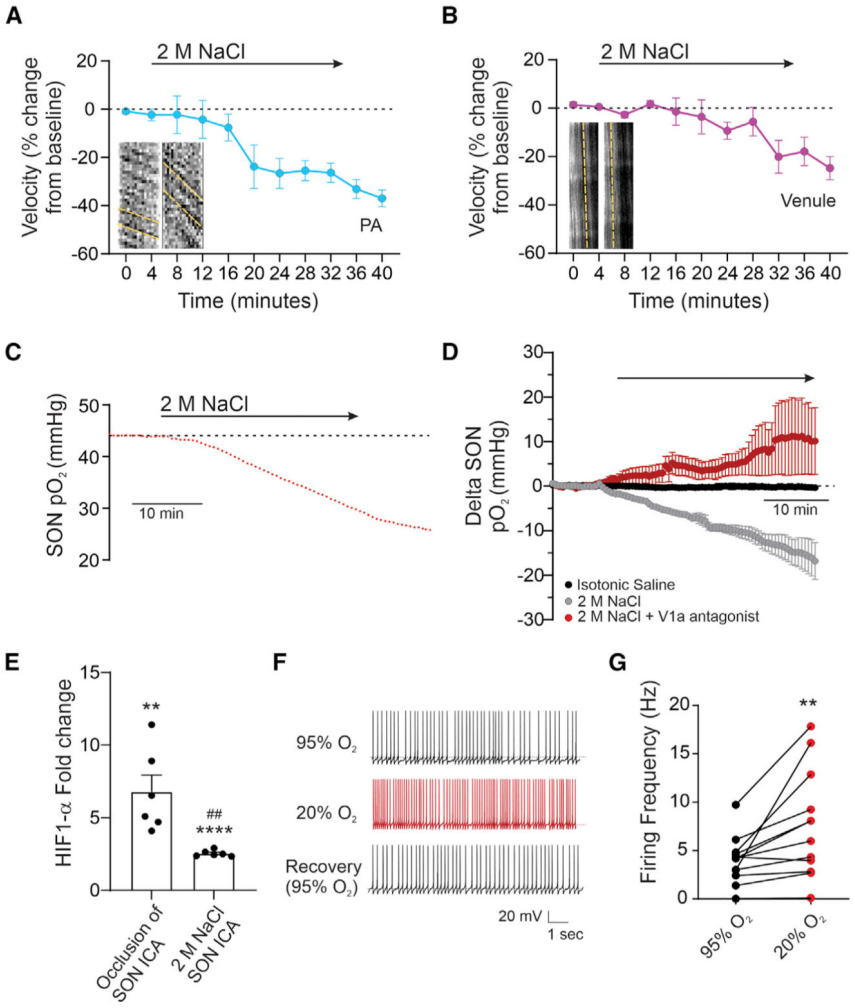

Figure 4. An acute salt load decreases blood flow in the SON, resulting in hypoxia and increased vasopressin neuronal firing activity

(A and B) Plots of mean changes in blood velocity as a function of time during the HTS infusion (i.v.; 1 mL; 30 min) in PAs (A; n = 4; F = 9.788; $p < 0.0001$) and venules (B; n = 4; F = 4.896; $p < 0.001$), respectively. Insets show corresponding representative kymographs obtained before (left) and at the peak (right) of the HTS infusion. Note the decreased slope of the stacks (yellow dashed lines) during the HTS infusion for both arteriole and venule.

(C) Representative raw trace showing changes in SON tissue partial pressure of oxygen (pO_2) before and during the HTS infusion.

(D) Summary of changes in the mean delta pO_2 during the HTS infusion (gray; n = 6; F = 17.8; p = 0.002), during an infusion of isotonic saline (black; n = 4; F = 0.4; p = 0.6), and during the HTS infusion in the presence of the V1a antagonist (red; n = 4; F = 1.85; p = 0.002).

(E) Summary of the mean fold change in HIF-1α mRNA expression in the SON following a partial occlusion of the ICA (left; n = 6; $^{**}p < 0.001$ versus contralateral control side; t = 17.7) and during the HTS infusion (right; n = 6; $^{***}p < 0.001$ versus isotonic saline; t = 5.0); $^{\#\#}p < 0.01$ versus ICA occlusion (t = 3.66).

Author Manuscript Author Manuscript Author Manuscript Author Manuscript

(F) Representative examples of firing activity recorded from an EGFP-VP neuron in slices showing a robust increase in firing discharge during a transient hypoxic stimulation (artificial cerebrospinal fluid [aCSF] 95% O_2 to aCSF 20% O_2).
(G) Plots of EGFP-VP neuronal mean firing rate in individual neurons in control (95% O_2) and hypoxic (20% O_2) conditions. **$p < 0.02$ versus 95% O_2 ($n = 14$; paired t test; $t = 3.66$). Error bars represent SEM.

Author Manuscript Author Manuscript Author Manuscript Author Manuscript

KEY RESOURCES TABLE

REAGENT or RESOURCE	SOURCE	IDENTIFIER
Chemicals, peptides, and recombinant proteins		
Urethane	Sigma	U2500–100G
Rhodamine	Sigma-Aldrich	R9379–100MG
Fluorescein 70 kDa dextrans	Sigma-Aldrich	46945–100MG-F
Alexa Fluor 633	Thermo Fisher Scientific	A30634
Acetylcholine	Sigma	A6625–25G
V1a receptor antagonist (β-mercaptob-β,β-cyclopenta methylene propionyl)	Sigma-Aldrich	V2255–1MG
Pentobarbital	Virbac	ANADA#200–071
Tetrodotoxin	Alomone Labs	T-500
Experimental models: organisms/strains		
Transgenic eGFP-VP Wistar rats	Provided by Dr. Yoichi Ueta (School of Medicine, University of Occupational and Environmental Health, Kitakyushu, Japan).	Ueta et al., 2005.
Oligonucleotides		
Beta-actin (rat)	QIAGEN	QT01830458
HIF-1α (rat)	QIAGEN	QT00193473
Software and algorithms		
Prism 8	Graphpad Prism	V9.2.0
Labchart 8	ADInstrument	S/N: 109058
PrairieView	Bruker	Version 5.5
Other		
miRNAeasy Mini kit	QIAGEN,	Cat. No. 217004
QIAzol Lysis Reagent	QIAGEN	Cat. No. 1023537
cDNA Synthesis Kit	BIO RAD	Cat. No. 1725035